Line-field confocal optical coherence tomography based on tandem interferometry with a focus-tunable lens

Flora Latriglia, Jonas Ogien, Arnaud Dubois

Research Article | Vol. 15, No. 9 / 1 Sep 2024 / Biomedical Optics Express 5384
Biomedical Optics EXPRESS

Line-field confocal optical coherence tomography based on tandem interferometry with a focus-tunable lens

FLORA LATRIGLIA,[1,2] JONAS OGIEN,[2] AND ARNAUD DUBOIS[1,2,*]

[1] *Université Paris-Saclay, Institut d'Optique Graduate School, Centre National de la Recherche Scientifique, Laboratoire Charles Fabry, 91127 Palaiseau, France*
[2] *DAMAE Medical, Paris, France*
info@damae-medical.com
[*] *arnaud.dubois@universite-paris-saclay.fr*

Abstract: This article introduces an innovative line-field confocal optical coherence tomography (LC-OCT) system based on tandem interferometry, featuring a focus-tunable lens for dynamic focusing. The principle of tandem interferometry is first recalled, and an analytical expression of the interferometric signal detected is established in order to identify the influence of key experimental parameters. The LC-OCT system is based on a Linnik-type imaging interferometer with a focus-tunable lens for focus scanning, coupled to a Michelson-type compensating interferometer using a piezoelectric linear translation stage for coherence plane scanning. The system achieves axial and lateral image resolutions of approximately 1 µm over the entire imaging depth (400 µm), in line with conventional LC-OCT. Vertical section images (B-scans) of skin acquired at 14.3 fps reveal distinguishable structures within the epidermis and dermis. Using refocusing and stitching, images of a tissue phantom were obtained with an imaging depth superior to 1.4 mm. The system holds promise for LC-OCT miniaturization, along with enhanced imaging speed and extended imaging depth.

1. Introduction

Line-field confocal optical coherence tomography (LC-OCT) is an interferometric imaging technique derived from time-domain OCT (TD-OCT) [1]. This technology has demonstrated its efficacy in the field of dermatology, capable of providing images of the skin with cellular resolution [2–4]. Unlike conventional TD-OCT, which employs point scanning and point detection, LC-OCT uses line illumination and line detection [2,5]. LC-OCT generates B-scans (vertical section images) by capturing multiple A-scans simultaneously using a line scan camera. Axial image resolution of approximately 1 µm at a central wavelength of about 800 nm is achieved by utilizing a supercontinuum laser as the light source and carefully balancing chromatic dispersion between the interferometer arms. LC-OCT takes advantage of a confocal gate produced by the line-scan camera, optically conjugated with the illumination line, in combination with a high numerical aperture microscope objective. This confocal gate enables LC-OCT to image highly scattering tissues, such as skin, down to a depth of around 500 µm.

Line illumination has been implemented in frequency-domain OCT (FD-OCT). Swept-source OCT (SS-OCT) with line illumination offers a substantial advantage in terms of image acquisition speed and detection sensitivity compared to TD-OCT, with high-speed systems operating around 100 times faster than LC-OCT, for the same pixel density per B-scan [6]. However, axial resolution in SS-OCT is typically around 5 µm in biological tissues, limited by the restricted spectral range of tunable light sources available in the spectral regions around 800 nm and 1060 nm. Line illumination has also been implemented in spectral-domain OCT (SD-OCT),

#530717 https://doi.org/10.1364/BOE.530717
Journal © 2024 Received 21 May 2024; revised 26 Jul 2024; accepted 7 Aug 2024; published 19 Aug 2024

Biomedical Optics EXPRESS

enabling the capture of a B-scan in a single acquisition using a spectrometer and an area camera [7–11]. Line-field SD-OCT systems can achieve axial resolutions in the micrometer range, thanks to the availability of light sources with low temporal coherence. Nevertheless, both SS-OCT and SD-OCT face an intrinsic limitation concerning lateral resolution, as the focus cannot be dynamically adjusted during the parallel acquisition of the depth information [12,13].

In LC-OCT, multiple A-scans are acquired simultaneously, eliminating the need to scan the beam laterally to obtain a B-scan; instead, only axial scanning is required. The speed of axial scanning is therefore equal to the speed of B-scan acquisition. This allows for dynamic focus adjustment at a considerably lower speed than it would be needed with conventional point-scanning TD-OCT [2,3]. A high numerical aperture lens, such as a microscope objective, can thus be dynamically focused for high lateral resolution imaging in real time. To generate a B-scan in LC-OCT, the coherence plane (plane orthogonal to the optical axis of the objective, corresponding to a zero optical path difference) is scanned in depth while adjusting the focus of a microscope objective dynamically so that the coherence plane is continuously in-focus [2,3]. This requires the focus of the microscope objective to coincide with the coherence plane as the sample is scanned in depth. Most LC-OCT prototypes have employed a Linnik-type interferometer using two identical immersion microscope objectives, one in the reference arm and the other in the sample arm. The entire interferometer was placed on a piezoelectric translation stage (PZT stage) for depth scanning. However, this configuration has drawbacks. Two microscope objectives, a beam-splitter and the associated integration mechanics represent a significant total mass to be moved, which limits scanning speed and range due to inertia. Moreover, the PZT stage is bulky and heavy, which limits the compactness and lightness of a handheld LC-OCT probe. In an attempt to overcome these limitations, an LC-OCT prototype based on a Mirau interferometer was reported [14,15]. It aimed to reduce size, weight, and speed constraints associated with Linnik-based LC-OCT devices. However, an illumination power about ten times higher than that in the Linnik configuration was necessary, due to the beam obstruction caused by the reference mirror in the Mirau interferometer. Furthermore, the Mirau-based LC-OCT device still encountered scanning speed and amplitude issues due to the mass to be moved via a PZT stage.

The elimination of moving components in the LC-OCT interferometer would offer a potential solution to current challenges concerning acquisition speed and imaging depth. This could also open up new perspectives in terms of compactness and lightness of handheld LC-OCT probes. This can be achieved by performing the mechanical scan in a second interferometer operating in tandem with the interferometer of the LC-OCT imaging device. The capability of low-coherence tandem interferometry was initially demonstrated for metrology applications, especially in determining the group refractive index and thickness of a sample [16–19]. Low-coherence tandem interferometry has also found applications in the field of biomedical imaging, being implemented in full-field optical coherence tomography (FF-OCT). The FF-OCT technique is based on TD-OCT using a broadband light source with low spatial coherence to uniformly illuminate the surface of the sample and an area camera to acquire *en face* images, *i.e.* parallel to the surface of the sample [20,21]. To the best of our knowledge, all FF-OCT systems reported in tandem configuration could only acquire *en face* images at a fixed or adjustable depth; they did not allow real-time B-scan image acquisition due to the absence of high-speed dynamic focus scanning. The reported tandem-based FF-OCT systems have employed Michelson, Linnik, or Fabry-Perot interferometers as compensating interferometers and Linnik or Fizeau interferometers as imaging interferometers [22–27].

In this paper, we introduce a tandem-based LC-OCT system employing a Michelson interferometer as the compensating interferometer coupled by an optical fiber to a Linnik interferometer as the imaging interferometer. The configuration features a PZT stage in the compensating interferometer for coherence plane scanning and a focus-tunable lens (FTL) in the imaging

Biomedical Optics EXPRESS

interferometer for high-speed dynamic focus scanning [12,13,28–30]. The performance of the system is reported in comparison to a conventional LC-OCT system based on a single Linnik interferometer [2,3]. B-scan images of skin captured *in vivo* using this system are shown. We demonstrate that the use of an FTL in a tandem-based LC-OCT device has the potential to greatly extend the limits of imaging depth and acquisition speed in LC-OCT. In addition, integrating the imaging interferometer into a handheld probe would provide a lighter, more compact LC-OCT imaging system.

2. Principle of tandem interferometry

Before delving into the implementation and applications of tandem interferometry for LC-OCT, let us examine its theoretical functioning to grasp the optical principles involved. Oh *et al.* presented an analytical study of the interference signal acquired by the camera at the output of a tandem FF-OCT system [22]. Meanwhile, Latrive *et al.* provided an explanation of tandem interferometry based on spectral analysis [25]. Xu *et al.* introduced a mathematical framework describing the working principle of cascade optical coherence tomography (C-OCT), tailored for the purpose of freeform optics metrology [31]. In this technique, a secondary interferometer is connected in cascade to a primary interferometer where the freeform sample is positioned. The secondary interferometer operates on the principle of Fourier transform spectroscopy. Additionally, Tang *et al.* proposed an explanation of tandem interferometry based on an analysis of optical paths within the system [32,33]. Drawing inspiration from these prior studies, we propose to establish an analytical expression for the signal detected in tandem interferometry. Our study is illustrated through a numerical simulation and diagrams depicting the interfering beams.

A diagram of an imaging system based on tandem interferometry is shown in Fig. 1.

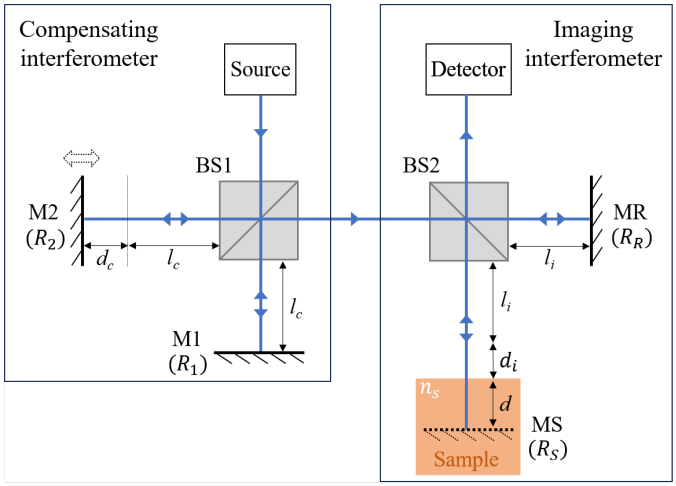

Fig. 1. Schematic diagram of an imaging system based on tandem interferometry. BS1, BS2: beam-splitters; M1, M2: mirrors of the compensating interferometer; MR, MS: reflective surfaces of the imaging interferometer; R_1, R_2, R_R, and R_S: reflection coefficients of M1, M2, MR, and MS; l_c, l_i: distances travelled in both arms of the compensating interferometer and the imaging interferometer, respectively; d_c, d_i: distances travelled in one arm of the compensating interferometer and in the imaging interferometer, respectively; d: imaging depth in the sample; n_s: refractive index of the sample.

The system, situated in air, comprises a compensating interferometer and an imaging interferometer, both of the Michelson type. The light source emits a collimated beam. We consider a

Biomedical Optics EXPRESS

polychromatic plane wave illuminating the interferometer, with complex amplitude given by:

$$U = s(k,\omega)e^{i(kr-\omega t)}, \tag{1}$$

where $s(k,\omega)$ represents the amplitude of the wave, as a function of the wave number k and the angular frequency ω, at time t and position r.

The beam initially passes through the compensating interferometer. A 50:50 beam-splitter, denoted as BS1, directs one beam to mirror M1, located at a fixed distance l_c from BS1. The second beam is directed to mirror M2, situated at a variable distance $l_c + d_c$ from BS1. The optical path length difference (OPD) is denoted $\delta_c = 2d_c$. The reflection coefficients of mirrors M1 and M2 are denoted as $R_1 = |r_1|^2$ and $R_2 = |r_2|^2$, respectively. The complex amplitudes of the two waves reflected by mirrors M_1 and M_2, after returning to BS1 are, respectively:

$$U_1 = \frac{U}{\sqrt{2}} r_1 e^{i(2kl_c)} \tag{2}$$

$$U_2 = \frac{U}{\sqrt{2}} r_2 e^{i(2k(l_c+d_c))} \tag{3}$$

The complex amplitude of the resultant wave after recombination by beamsplitter BS1 is:

$$U_{\text{comp}} = \frac{1}{\sqrt{2}}(U_1 + U_2) \tag{4}$$

The beam emerging from the compensating interferometer is then directed to the second interferometer (imaging interferometer), where it is again split in two by a 50:50 beam-splitter (BS2). Mirror MR, representing the reference surface of the imaging interferometer, is positioned at a fixed distance l_i from BS2. Mirror MS, representing the reflectivity of the plane to image within the sample, is situated at a fixed distance $l_i + d_i + n_s d$ from BS2, with n_s the refractive index of the sample, considered as constant. d_i is fixed and d is the imaging depth. The OPD in the imaging interferometer is $\delta_i = 2(d_i + n_s d)$. The reflection coefficients of mirrors MR and MS are denoted as $R_R = |r_R|^2$ and $R_S = |r_S|^2$, respectively. The complex amplitudes of the waves reflected by mirrors *MR* and *MS* are, respectively:

$$U_R = \frac{U_{\text{comp}}}{\sqrt{2}} r_R e^{i(2kl_i)} \tag{5}$$

$$U_S = \frac{U_{\text{comp}}}{\sqrt{2}} r_S e^{i(2k(l_i+d_i+n_s d))} \tag{6}$$

The complex amplitude of the resultant wave after recombination by BS2 is:

$$U_{\text{im}} = \frac{1}{\sqrt{2}}(U_R + U_S) \tag{7}$$

The spectral power density of the light at the output of the imaging interferometer is given by:

$$P(k) = U_{\text{im}} U_{\text{im}}^* \tag{8}$$

By substituting the previous equations, expanding, and simplifying, the expression becomes:

$$\begin{aligned} P(k) = \frac{UU^*}{16}\Gamma\Big[1 &+ \gamma_c \cos\left(2kd_c\right) \\ &+ \frac{\gamma_c\gamma_i}{2}\cos\left(2k(d_c + d_i + n_s d)\right) + \frac{\gamma_c\gamma_i}{2}\cos\left(2k(d_c - (d_i + n_s d))\right) \\ &+ \gamma_i \cos\left(2k(d_i + n_s d)\right)\Big] \end{aligned} \tag{9}$$

with:

Biomedical Optics EXPRESS

- Γ, a constant term depending on the reflection coefficients:

$$\Gamma = \frac{(R_1 + R_2)(R_S + R_R)}{16}. \tag{10}$$

- γ_c the contrast of the interference in the compensating interferometer :

$$\gamma_c = 2\frac{\sqrt{R_1 R_2}}{R_1 + R_2}. \tag{11}$$

- γ_i the contrast of the interference in the imaging interferometer :

$$\gamma_i = 2\frac{\sqrt{R_S R_R}}{R_S + R_R}. \tag{12}$$

Assuming that the detector has a flat spectral response, the measured intensity as a function of d_c is obtained by integration of the spectral power density expressed in Eq. (10) over the wave numbers:

$$I_{tandem}(d_c) = \int_0^\infty P(k)\, dk \tag{13}$$

We suppose the spectral intensity of the light source, $S(k)$, to be described by a Gaussian-shaped function of width Δk, centered at $k = k_0$:

$$S(k) = UU^* = S_0 \exp\left[-4\ln 2\left(\frac{k - k_0}{\Delta k}\right)^2\right] \tag{14}$$

Utilizing Fourier analysis, the final expression of the optical intensity detected at the output of the tandem interferometer can be derived:

$$\begin{aligned} I_{\text{tandem}}(d_c) = I_0\,\Gamma\Bigg[&1 + \gamma_c\,\gamma_{coh}(d_c)\cos(2k_0 d_c) \\ &+ \frac{\gamma_c\gamma_i}{2}\,\gamma_{coh}(d_c + d_i + n_s d)\cos\Big(2k_0(d_c + d_i + n_s d)\Big) \\ &+ \frac{\gamma_c\gamma_i}{2}\,\gamma_{coh}\big(d_c - (d_i + n_s d)\big)\cos\Big(2k_0\big(d_c - (d_i + n_s d)\big)\Big) \\ &+ \gamma_i\,\gamma_{coh}(d_i + n_s d)\cos\Big(2k_0(d_i + n_s d)\Big)\Bigg] \\ = I_0\,\Gamma\,&(1 + T_1 + T_2 + T_3 + T_4) \end{aligned} \tag{15}$$

with :

- I_0, the source intensity, given by a Gaussian integral:

$$I_0 = \int_0^\infty S(k)\, dk = S_0\frac{\Delta k}{2}\sqrt{\frac{\pi}{\ln 2}}; \tag{16}$$

- γ_{coh}, the temporal coherence function:

$$\gamma_{coh}(z) = \exp\left[-4\ln 2\left(\frac{z}{\Delta z}\right)^2\right] \tag{17}$$

where Δz is the axial resolution (in air) of the imaging device, defined as the full width at half maximum (FWHM) of the temporal coherence function : $\Delta z = \frac{4\ln 2}{\Delta k}$ [34].

Biomedical Optics EXPRESS

Figure 2(a) displays a plot (in purple) of $I_{tandem}(d_c)$, according to Eq. (7), considering the following parameters: $n_s = 1.4$, $d_i = 5\mu$m, $d = 10\mu$m, $R_1 = R_2 = 1$. To approach the reflectivity of the skin and that of the reference surface in our tandem-based LC-OCT system, we take $R_S = 1\%$ and $R_R = 4\%$. The source spectrum is considered Gaussian centered at wavelength $\lambda_0 = 800$nm, with a FWHM of $\Delta\lambda = 200$nm, giving $k_0 = \frac{2\pi}{\lambda_0} = 7.8\mu\text{m}^{-1}$ and $\Delta k = 2\pi\frac{\Delta\lambda}{\lambda_0^2} = 1.9\mu\text{m}^{-1}$.

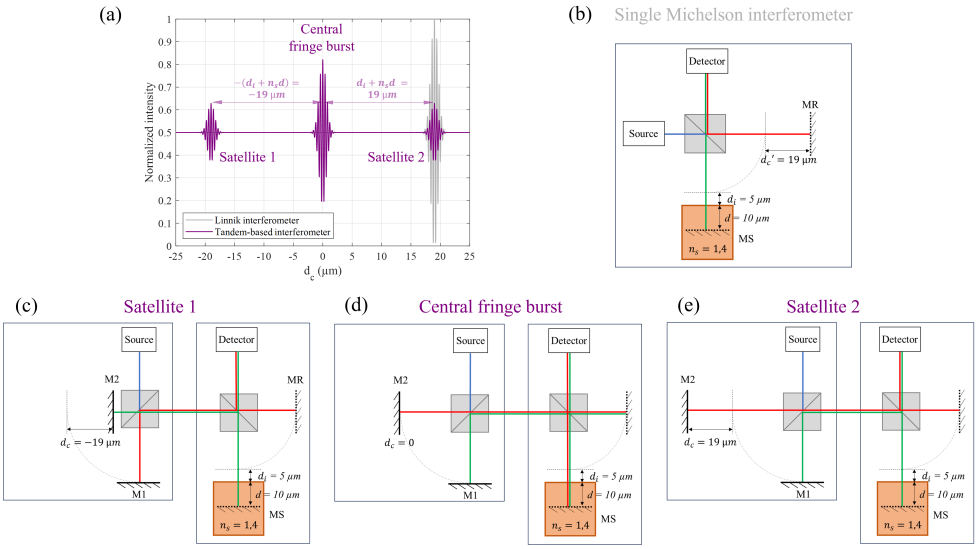

Fig. 2. (a) Theoretical optical intensity at the output of a tandem interferometer, calculated using Eq. (7) (in purple). The case of a single Michelson interferometer is shown for comparison (in gray). The parameters of the simulation are: $d_i = 5\mu$m, $d = 10\mu$m, $n_s = 1.4$ and $R_1 = R_2 = 1$, $R_R = 4\%$ and $R_S = 1\%$. (b) Schematic diagram of the interfering beams in a Linnik interferometer, shown in green and red. (c), (d) and (e) Schematics showing the variable distance d_c and the rays that interfere (shown in red and green) to form satellite 1 (c), the central burst (d) and satellite 2 (e).

The interpretation of terms T_1, T_2, T_3 and T_4 is given below:

- Term T_1 describes interferences occuring in the compensating interferometer alone. Those interferences occur when $d_c \sim 0$, *i.e.* around a null optical path difference in the compensating interferometer. As depicted in Fig. 2(d), the beam emitted by the light source is split in two by the beam-splitter in the compensating interferometer. After reflection on mirrors M1 and M2, these two beams are recombined by the same beam-splitter and interfere because the two arms of the compensating interferometer have roughly equal lengths. The two interfering beams are then sent to the imaging interferometer, where they are both reflected by the reference mirror (MR) and the sample (MS). The imaging interferometer, whose arms have very different optical lengths, is not involved in those interferences.

- Term T_2 corresponds to the interference pattern named "satellite 1" (see Fig. 2(c)). Its envelope, given by $\gamma_{coh}(d_c + d_i + n_s d)$, reaches its maximum at $d_c = -(d_i + n_s d)$. Here both interferometers are involved in the detected interference, operating in tandem. The beams contributing to the formation of satellite 1 are depicted in Fig. 2(c). The beams drawn in green and red do not travel the same optical path length in the imaging interferometer. Without the compensating interferometer, they would not interfere. The optical paths difference of the red and green beams in the compensating interferometer compensate the

Biomedical Optics EXPRESS

optical paths difference in the imaging interferometer so that the two beams travel the same optical paths after being recombined by the beam-splitter in the imaging interferometer. The two interferometers work in tandem, mutually compensating for the differences in optical paths present in each of them.

- The same principle of optical path compensation applies to beams contributing to the formation of satellite 2 (Fig. 2(a) and 2(e)). This satellite corresponds to term T_3, which is centered at $d_c = d_i + n_s d$. By examining the expression of I_{tandem}, it appears that the amplitudes of terms T_2 and T_3 are reduced by a factor of $\frac{\gamma_i}{2}$ compared to term T_1, as shown in Fig. 2(a).

- Term T_4 represents the interference occurring in the imaging interferometer alone. As the optical path difference in the imaging interferometer is fixed and in practice much greater than the width of the temporal coherence function, this term is constant and close to zero ($\gamma_{coh}(d_i + n_s d) \sim 0$).

For comparison, the interferogram at the output of a single interferometer (shown in Fig. 2(b)) was also simulated (see Fig. 2(a), in gray). The imaging arm of the interferometer is the same as that of the imaging interferometer in the tandem system, but its reference mirror is located at distance $l_i + d'_c$ from the beam-splitter. As a result, the optical path length difference between the two arms is $\delta_M = 2(d'_c - d_i - n_s d)$. The FWHM of the envelope of satellite 2 (and satellite 1) is the same as that of the interference pattern at the output of the single interferometer, which means that axial resolution is maintained in the tandem-based LC-OCT imaging system. However, for reflection coefficients $R_R = 4\%$ and $R_S = 1\%$, the amplitude of satellite 2 (and satellite 1) is 5 times lower than that of the interferogram at the output of a single interferometer. This highlights the reduction in interference contrast caused by the use of tandem interferometry. The impact of the reduction in interferometric signal amplitude on image quality will be discussed later.

The principle of tandem interferometry is used in the LC-OCT system presented in this paper. A vertical section image (B-scan) of a sample is obtained from the interferometric signal corresponding to one of the two satellites. Scanning the imaging depth d is achieved by varying distance d_c in the compensating interferometer by axial translation of mirror M2. The distance between the satellites and the central fringe burst must be greater than the depth range probed in the sample to avoid artefacts in the images. It is set through distance d_i by adjusting the position of mirror MR. In the imaging interferometer, only the focus has to be dynamically adjusted to be superimposed with the coherence plane. This is achieved using a focus-tunable lens, as will be explained below.

3. Experimental setup

The experimental setup of the tandem-based LC-OCT device with a focus-tunable lens (FTL) is shown schematically in Fig. 3.

3.1. Compensating interferometer

The compensating interferometer is a Michelson interferometer. A supercontinuum fiber laser (NKT photonics, SuperK EVO) serves as the broadband spatially-coherent light source, operating at a central wavelength of approximately 800 nm. Light emitted from the source is collimated and subsequently sent into the two interferometer arms via a 50:50 non-polarizing beam-splitter (Thorlabs, BS014). In each of these arms, the beam is reflected by a silver-coated mirror (Thorlabs, PF05-03-P01). The position of mirror M1 is adjustable in the y-axis. Conversely, mirror M2 is mounted on a PZT linear translation stage (Physik Instrument, P625.1CD) and oscillates in the x-axis for coherence plane scanning. The tilts of both mirrors are adjustable to facilitate injection into the single-mode fiber at the interferometer's output. This injection is

Biomedical Optics EXPRESS

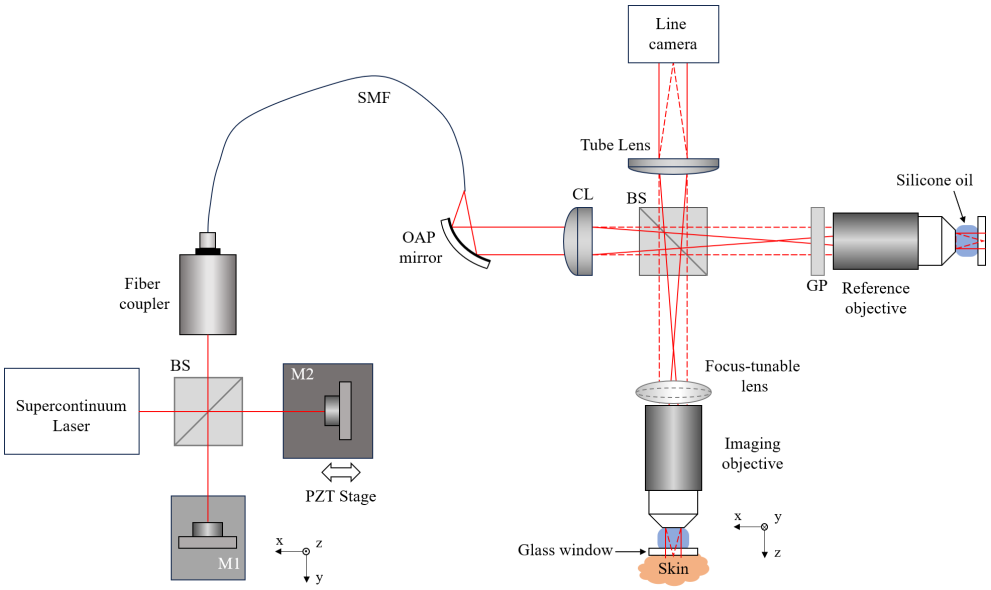

Fig. 3. Schematic diagram of the tandem-based LC-OCT system with a focus-tunable lens (FTL). BS: beam-splitter; PZT: piezoelectric (the double arrow represents the oscillation of the PZT linear translation stage); SMF: single mode fiber; OAP: off-axis parabolic mirror; CL: cylindrical lens; GP: glass plate. The dotted red lines in the imaging interferometer represent the beam in the direction orthogonal to the plane of the figure.

achieved using a collimator attached to a fiber coupler, directly connected to the single-mode fiber (Excelitas Technologies, Qioptiq, kineFLEX).

3.2. Imaging interferometer

The imaging interferometer is of the Linnik type, with a microscope objective (Olympus, UMPLFLN 20XW, water immersion, 20X, numerical aperture of 0.5) placed in each of the two interferometer arms. Light transmitted by the optical fiber from the compensating interferometer passes through a collimator and a cylindrical lens to produce a line of light focused by the microscope objectives onto the sample and on a plane reference surface. A glass plate is introduced into the reference arm for dispersion compensation purposes, as will be explained in section 3.3. The images given by the objectives are formed onto the sensor of a line-scan camera (Octoplus, Teledyne e2v, 2048 pixels) using a tube lens (Thorlabs, AC254-150-B). Silicone oil, featuring a refractive index of 1.41, is employed as the immersion medium, closely approximating the mean refractive index of skin. A 500 µm-thick glass window is placed under each microscope objective, serving a dual purpose. In the reference arm, the window acts as a low reflectivity (3.5%) plane reference reflector. In the sample arm, the window stabilizes the skin pressed against it. Before skin imaging, a layer of paraffin oil (refractive index of 1.47) is deposited between the skin and the glass window to attenuate light scattering and reflection from both the skin surface and the glass window.

3.3. Focus-tunable lens for dynamic focus scanning

Dynamic focus scanning is performed using an FTL (EL-16-40-TC, Optotune) positioned directly above the infinity-corrected microscope objective in the sample arm. The FTL clear aperture is 16 mm, superior to the 10.7 mm clear aperture of the microscope objective. The FTL has a

Biomedical Optics EXPRESS

recommended optical power range of -2 diopters to +3 diopters, which corresponds to a focusing range of the microscope objective of 640 µm. The FTL features a near-infrared coating on its surfaces to minimize unwanted reflections. A current controller (ECC-1C, Optotune) is used to precisely adjust the focus of the FTL. The FTL weighs 40g, inserted in a mount measuring 40 mm in diameter and 11.9 mm in thickness. By comparison, the PZT linear stage has a mass of 240g and dimensions of 60 mm × 60 mm × 15 mm (length × width × thickness). Replacing the PZT linear stage with the FTL in the imaging interferometer therefore represents a significant gain in both compactness and weight.

To compensate for the chromatic dispersion introduced by the FTL, a glass plate (GP) is introduced into the reference arm of the imaging interferometer. The thickness of the plate is chosen to best compensate for the chromatic dispersion introduced by the FTL when its optical power is zero. While the fixed-thickness GP provides effective compensation when the FTL surfaces are flat (optical power zero), it does not offer an optimal solution when the FTL optical power is varied for focus scanning. Indeed, the optical path travelled within the FTL varies depending on the applied voltage. Nonetheless, we opted for a simple compensation method while paying particular attention to the measurement of the influence of dispersion on axial resolution to assess the system's performance (see section 4.1).

One of the interests of the tandem-based LC-OCT system with a FTL for focus scanning is the potential enhancement of image acquisition speed. The FTL can be operated at a frequency of several tens of Hertz for dynamic focusing over a range of -2 to +3 diopters. The coherence plane can be scanned in the compensating interferometer using a PZT linear stage at an increased frequency compared to conventional LC-OCT systems [2,3], as only a small mirror mounted on a tip/tilt adjustment is attached to the PZT stage, representing a lightweight load to move (~30g). Furthermore, the PZT stage oscillates horizontally, which cancels out the effects of gravity on the motion. The camera, with a maximum operating frequency of f_{cam} = 120 kHz, then becomes the limiting factor in acquisition speed. The PZT stage oscillates in an asymmetric triangular pattern with an amplitude resulting to a coherence plane scan amplitude of Z = 400 µm and a duty cycle of $D = 0.7$. Its frequency f_{PZT} is adjusted to generate an optical phase-shift of $\sim \pi/2$ between the acquisitions of two consecutive lines. This corresponds to a displacement of the coherence plane of $\delta = \frac{\lambda}{8n}$. Given the mean optical wavelength of the detected light (λ = 800 nm) and the refractive index of skin ($n \sim 1.4$), the frequency of the PZT oscillation for coherence plane scanning is set to:

$$f_{PZT} = \frac{D \times \delta \times f_{cam}}{Z} = 14.3Hz. \tag{18}$$

The oscillation frequency of the PZT stage corresponds to the B-scan acquisition frequency, *i.e.* the frame rate. In comparison, previously reported LC-OCT systems in the Linnik configuration operated at frame rates of 8-10 Hz [2,3].

The input signal directed to the FTL is adjusted to enable continuous optical power scanning (allowing for continuous scanning of the focusing plane in the skin) at frequency f_{PZT} = 14.3 Hz, following an asymmetric sawtooth waveform with a 75 % duty cycle (Fig. 4(a)).

The integrated FTL does not allow for direct monitoring of its actual optical power response to a given input signal. Consequently, we devised a method to monitor the focusing plane position over the optical power scan of the FTL, when driven as shown in Fig. 4(a). This method also allows to monitor the coherence plane position, as it is not directly equal to the PZT displacement considering that the mirror of the compensating interferometer is scanned in air, while the coherence plane is scanned within the skin. This method is detailed in the paragraph below.

To acquire a B-scan, the LC-OCT system scans the line of light in depth within the sample, while the line scan camera collects the reflected flux. A so-called two-dimensional "raw" image is generated by concatenating these individual one-dimensional images acquired by the camera into a stack. In such raw image, a reflective surface as a sample appears both as a set of interference

Biomedical Optics EXPRESS

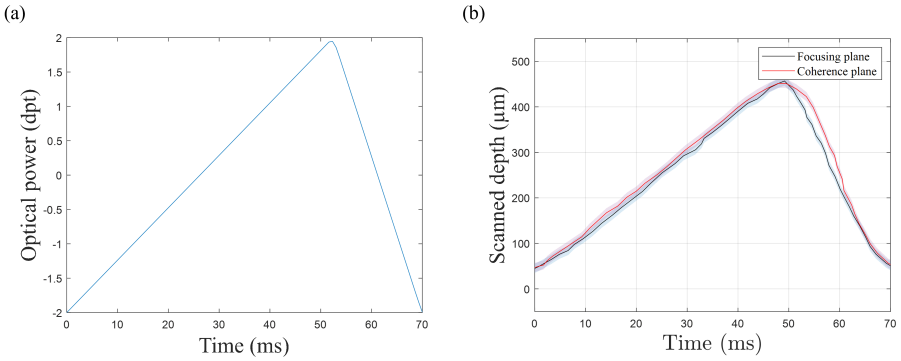

Fig. 4. Data and measurements for the coordination of focusing and coherence plane scans. (a) Signal sent to the EL-16-40-TC lens via the Optotune Cockpit software. (b) Measurements of the focusing and coherence plane positions over time.

fringes located in the vicinity of the coherence plan and as a broad line around the focusing plane (the width of this line in the axial direction corresponding to the depth of field of the microscope objective). This image enables us to determine if the coherence and focusing planes are aligned. It ensures that the FTL for focusing plane scanning and the PZT stage for coherence plane scanning are properly synchronized and calibrated. By imaging a plane interface at various depths, we can characterize the coherence plane's position and the focusing plane's position over the scans by both the PZT and the FTL, verifying their alignment (see Fig. 4(b)). In practice, we imaged the interface between the glass window and air in the sample arm, in the absence of a sample. Adjusting the depth of this interface also modifies the thickness of silicone oil downstream of the imaging objective, hence imitating a scan in the skin. The effective amplitude of the scanned depth is Z = 400 µm, corresponding to a range of -2 to +2 diopters for the FTL. Only images acquired during the slow positive ramps are used. A triggering signal is sent by the FTL at each cycle to synchronize the camera and the PZT stage.

During each positive slope of the depth scan, a stack of $Z/\delta = 5600$ lines is acquired. The generation of a vertical cross-sectional image (a B-scan) involves the application of a five-frame fringe envelope detection algorithm [35] to the acquired raw image [3,36]. This acquisition and data processing procedure is executed continuously throughout the oscillation cycles of the actuators. The resultant images are obtained after automatic contrast optimization following suitable rescaling. Each vertical cross-sectional image has 1707×680 pixels, corresponding to a field of view of 1 mm $\times$ 0.4 mm ($x \times z$).

4. System performance characterization

The optical performance of the system was assessed in comparison with the performance of the last Linnik-based LC-OCT systems reported in the literature [2,37].

4.1. Axial resolution

The axial response of the LC-OCT system was assessed by imaging the interface between the glass window and air in the sample arm, in the absence of a sample. The axial resolution was defined as the average full-width-at-half-maximum (FWHM) of the envelope of the interferograms acquired across the entire width of the image. Measurements were performed for different positions of the interface to evaluate how the axial resolution evolves with imaging depth (see Fig. 5), in particular to identify if it is affected by the change of state of the liquid lens over the scan.

Biomedical Optics EXPRESS

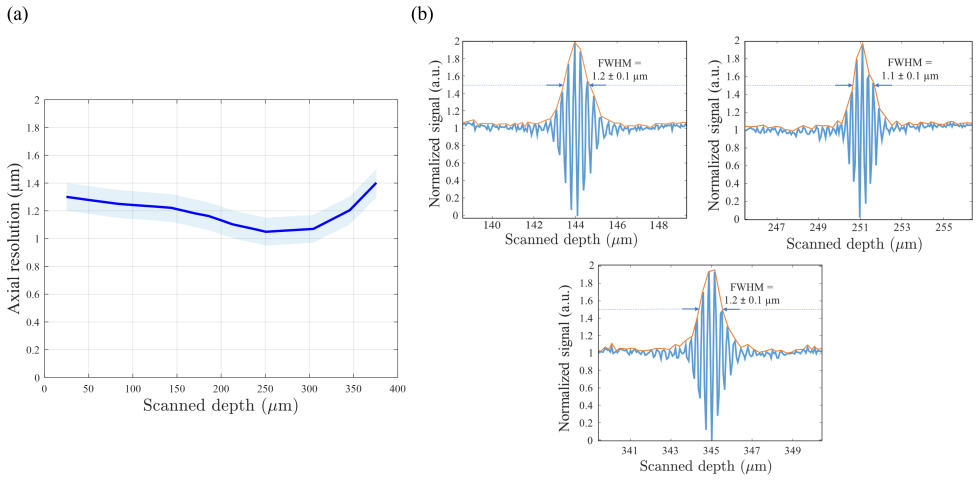

Fig. 5. Axial resolution measurements. (a) Measured axial resolution in μm as a function of imaging depth, also in μm. (b) Typical interference signal captured by a pixel of the line-scan camera when a planar interface is used as a sample, at depths of ca. 144 μm, 250 μm and 345 μm. The full width at half maximum (FWHM) of the fringe envelopes is measured.

The system's axial resolution was measured to be 1.2 ± 0.1 μm at a depth of 144 μm, 1.1 ± 0.1 μm at 250 μm, and 1.2 ± 0.1 μm at 345 μm. Even when considering the uncertainty intervals, the axial resolution does not exceed 1.5 μm. The theoretical axial resolution, considering a Gaussian-shaped spectrum centered at 800 nm with a FWHM of 200 nm, is 1.00 μm [1]. Discrepancies between the theoretical prediction and the experimental findings are attributed to the influence of spectral transmittance of optical components and the non-Gaussian shape of the detected spectrum, along with non-perfect dispersion compensation between the arms of the interferometer. The measured axial resolution closely corresponds to that reported in the Linnik configuration, yielding 1.15 μm [36]. The disparities in performance along the depth scan can be attributed to the fixed thickness of the glass plate placed in the imaging interferometer to compensate for the dispersion induced by the FTL. The thickness of the compensating glass plate was optimized for a FTL focal power of 0 diopters (zero optical power applied). Since the FTL focal power varies between -2 and +2 diopters over the scan, the axial resolution varies with depth due to dispersion mismatch and reaches its best value at a depth where the dispersion compensation is optimized (around 250 μm here). Note that the depth with the best resolution can be adjusted through optimization of the glass plate thickness or through the signal sent to the variable-focus lens. However, the axial resolution varies by no more than ~ 10% over the entire 400 μm scan depth.

4.2. *Lateral resolution*

The lateral resolution was assessed through imaging a resolution test target (Technologie Manufaktur, Resolution test target TC-RT01) at various imaging depths. Profiles of different line pattern groups were traced from raw images to evaluate the highest resolution profile displaying sufficient contrast for distinction (Fig. 6). This profile corresponded to the line pattern group of 500 lp/mm. A reduction of the contrast was observed with increasing imaging depth. The line pattern group of 500 lp/mm corresponds to a lateral resolution of 1.0 μm. Although the microscope objective is not used in infinite-conjugate configuration over most of the scan by the FTL, the measured lateral resolution is consistent with previously reported measurements using the same microscope objective immersed in silicone oil in infinite-conjugate configuration

Biomedical Optics EXPRESS

[36]. Consequently, we infer that the impact on optical aberrations of using silicone oil instead of water as the immersion medium is greater than not using the objectives in infinite-conjugate configuration. The use of the FTL does not further degrade lateral resolution.

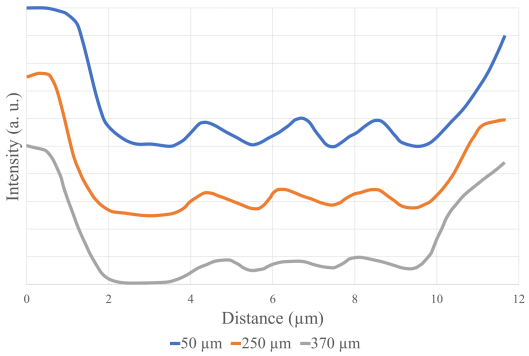

Fig. 6. Intensity profiles measured for imaging depths of 50 μm, 250 μm, and 370 μm.

4.3. *Depth of field*

Restricting the depth of field (DOF) enhances confocal filtering, which diminishes the impact of reflective out-of-focus sample structures on image quality. In order to evaluate if the use of the FTL affects the confocal filtering of the LC-OCT system, the DOF was evaluated across the scan of the FTL. The DOF can be directly evaluated by measuring the width in the axial direction (FWHM) of the bright line corresponding to the focusing plane in raw images. For ease of measurement, the reference arm in the imaging interferometer was obstructed to retain only the signal from the sample. The DOF was determined by the average of the FWHM of the focusing plane across the entire width of the image. By displacing the imaged interface in depth, the DOF was measured as a function of depth (Fig. 7). The DOF remains stable across the entire imaging depth, ranging from 12.6μ*m* to 14.6μm, accounting for measurement uncertainties. The scan by the FTL, therefore, has no significant impact on the DOF.

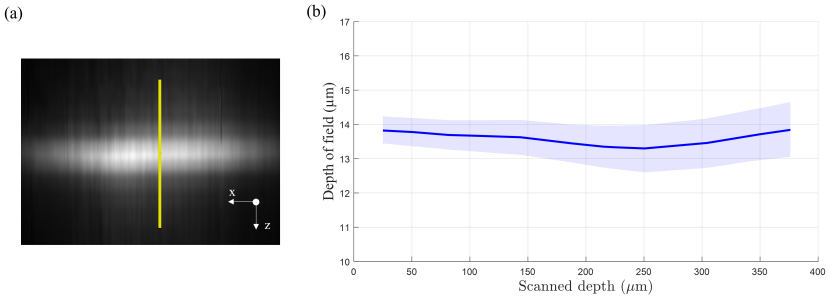

Fig. 7. (a) Raw image of a planar reflector (without interference). The yellow line indicates the position of the intensity depth profile considered to measure the depth of field. (b) Depth of field as a function of depth, measured from the width (FWHM) of the intensity depth profile as a function of the position of the planar reflector.

Biomedical Optics EXPRESS

5. Results and perspectives

5.1. In vivo skin imaging

In vivo imaging of human skin was conducted to demonstrate the system's performance. Figure 8(a) and 8(b) present B-scan images of healthy skin captured at an imaging rate of 14.3 frames per second (fps), taken from a 26-year-old woman's back of the hand (Fig. 8(a)) and tip of the index finger (Fig. 8(b)). The images distinctly reveal the epidermis (E) and the dermis (D), separated by the dermal-epidermal junction (DEJ). In the epidermis, the stratum corneum (SC) is discernible. It is particularly thick on the tip of the index finger (Fig. 8(b)). Notably, the nuclei of keratinocyte cells (K) in the epidermis are resolved and appear as dark spots in the images. Additionally, the dermis exhibits distinguishable features such as collagen fibers (CF) and blood vessels (BV). Other structures, including a sweat duct (SD), are also observable. The images are similar to those obtained with the Linnik-based LC-OCT devices [2,3,36]. The contrast loss induced by the utilization of a tandem-based LC-OCT system (see discussion in section 2) and the use of an FTL for dynamic focusing ultimately appear to have no significant impact on image quality. Although a spatially coherent light source is used, no obvious speckle-related artifacts can be observed in the images. Possible reasons for this are discussed in [14]. In particular, sample movements during *in vivo* imaging generate phase variations whose average over the interferometric image acquisition time (~10µs) attenuates the effect of speckle.

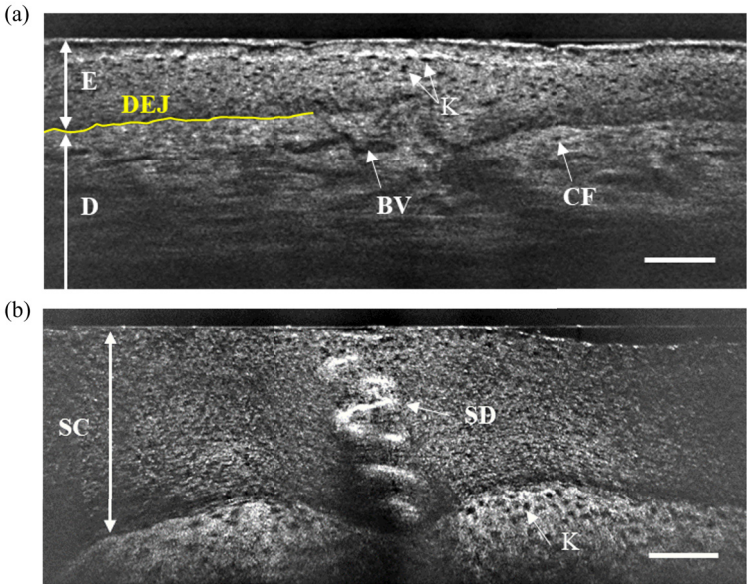

Fig. 8. Tandem-based LC-OCT B-scan images of human skin, *in vivo*, acquired at 14.3 fps. (a) Back of the hand. (b) Tip of the index. E: epidermis; D: dermis; SC: stratum corneum; K: keratinocyte; DEJ: dermal-epidermal junction; SD: sweat duct; CF: collagen fibers; BV: blood vessels. Scale bars: 100 µm.

5.2. Expansion of imaging depth

The imaging depth of the system is limited to 400 µm by the oscillation range of the PZT stage for coherence plane scanning. However, the FTL offers the possibility of adjusting the focusing plane beyond 400 µm depth. To assess the range of imaging depths achievable with the FTL, acquisitions were performed using a dedicated setup and a sample made of a polydimethylsiloxane

Biomedical Optics EXPRESS

(PDMS) matrix in which titanium dioxide (TiO_2) particles were embedded. This sample has a refractive index close to the one of skin [38]. The PZT stage was oscillated through its maximum range around a position x_1. A series of 16 images was acquired by progressively varying the constant voltage applied to the FTL. These images correspond to foci evenly spaced in depth over the 400 µm range. The PZT stage, mounted on a manual translation stage, was then moved manually to reach a new position $x_2 = x_1 + 400\mu m$. This whole procedure was repeated 4 times. The optical powers of FTL was varied from -4.5 diopters to 2.5 diopters. For correction of chromatic dispersion, the same glass plate as used in the proof-of-concept assembly was employed, with no specific adjustments. The resulting 64 images acquired were then combined to construct a final image corresponding to a depth range of 1410 µm. This principle of image recombination has already been applied and has proved effective in frequency-domain OCT [12,13] and TD-OCT [39]. One of the individual images, along with the combination of all the individual images, are shown in Fig. 9. The imaging depth of 1410 µm is 3 times larger than that reached with conventional LC-OCT, with no visible loss of resolution. The use of the FTL thus opens new perspectives in terms of imaging depth range.

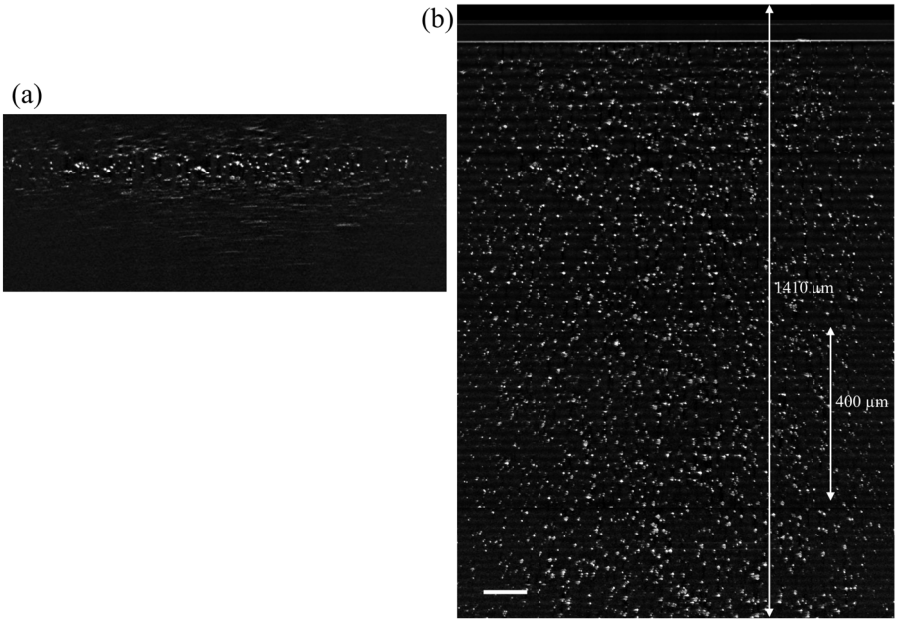

Fig. 9. Images of a sample made of titanium dioxide ($Ti0_2$) particles embedded in a polydimethylsiloxane (PDMS) matrix for assessment of the achievable depth range using the FTL. (a) Image acquired for a given optical power of the FTL. (b) Combination of all acquired images, with optical powers applied to the FTL spanning from -4.5 to 2.5 diopters. Scale bar: 100 µm.

6. Conclusion

An LC-OCT system based on tandem interferometry with a focus-tunable lens was demonstrated. The principle of tandem interferometry was first explained using a model of the detected signal based on wave optics. An interpretation of the principle of tandem interferometry in terms of optical paths was also provided. The demonstrated tandem-based LC-OCT device integrates a Michelson interferometer as the compensating interferometer and a Linnik interferometer as the imaging interferometer. Noteworthy features include the use of a PZT linear translation stage

Biomedical Optics EXPRESS

in the compensating interferometer for coherence plane scanning and a focus-tunable lens in the imaging interferometer for focus scanning. The elimination of a PZT stage in the imaging interferometer significantly improves its compactness and lightness. The optical performance of the system was studied, with axial and lateral resolutions measured close to 1 µm, aligning with conventional LC-OCT systems. Spatial resolution and depth of field were evaluated at various imaging depths, ensuring satisfactory image quality throughout the depth range with image dimensions of 1000 µm × 400 µm ($x \times z$). B-scan imaging of skin was performed, *in vivo*, revealing key structures of the epidermis and upper dermal layers. The loss of contrast of the interferometric signal resulting from the use of the tandem interferometer have not proven detrimental to *in vivo* skin imaging. The combination of tandem interferometry and use of a focus-tunable lens enabled an imaging speed of 14.3 fps, superior to Linnik-based LC-OCT systems reported to date. At this frame rate, the line-scan camera becomes the limiting factor in acquisition speed, which could be further increased by using a faster camera, provided that the light power sent onto the sample can be increased and that the PZT stage in the compensating interferometer can still oscillate linearly at the desired frequency. The impact of gravity on the operation of the FTL could be an issue if the imaging interferometer were to be integrated and used in a handheld probe. Progress in gravity-compensated FTL would provide a solution to this issue. The integration of the FTL into a handheld probe would maximize the compactness and lightness advantages achieved by the system. Finally, we demonstrated that the FTL could contribute to scan beyond 1400 µm depth, a more than 3-fold improvement compared to LC-OCT systems previously reported. Provided that a suitable actuator can be used to scan the coherence plane in the compensating interferometer, imaging would be possible at greater depths and speeds than current LC-OCT by means of a more compact and lighter device. This suggests promising advancements in LC-OCT technology for enhanced imaging capabilities.

Acknowledgments. The authors are grateful to the company DAMAE Medical for technical and financial supports.

Disclosures. The authors declare no conflict of interest.

Data availability. Data underlying the results presented in this paper are not publicly available at this time but may be obtained from the authors upon reasonable request.

References

1. A. G. Podoleanu, "Optical coherence tomography," J. Microsc. **247**(3), 209–219 (2012).
2. A. Dubois, O. Levecq, and H. Azimani, "Line-field confocal optical coherence tomography for high-resolution noninvasive imaging of skin tumors," J. Biomed. Opt. **23**(10), 1 (2018).
3. J. Ogien, A. Daures, and M. Cazalas, "Line-field confocal optical coherence tomography for three-dimensional skin imaging," Front. Optoelectron. **13**(4), 381–392 (2020).
4. F. Latriglia, J. Ogien, and C. Tavernier, "Line-field confocal optical coherence tomography (LC-OCT) for skin imaging in dermatology," Life **13**(12), 2268 (2023).
5. Y. Chen, S.-W. Huang, A. D. Aguirre, *et al.*, "High-resolution line-scanning optical coherence microscopy," Opt. Lett. **32**(14), 1971 (2007).
6. D. J. Fechtig, B. Grajciar, and T. Schmoll, "Line-field parallel swept source MHz OCT for structural and functional retinal imaging," Biomed. Opt. Express **6**(3), 716 (2015).
7. A. F. Zuluaga and R. Richards-Kortum, "Spatially resolved spectral interferometry for determination of subsurface structure," Opt. Lett. **24**(8), 519 (1999).
8. B. Grajciar, M. Pircher, A. F. Fercher, *et al.*, "Parallel Fourier domain optical coherence tomography for in vivo measurement of the human eye," Opt. Express **13**(4), 1131 (2005).
9. Y. Nakamura, S. Makita, and M. Yamanari, "High-speed three-dimensional human retinal imaging by line-field spectral domain optical coherence tomography," Opt. Express **15**(12), 7103 (2007).
10. S. Lawman, Y. Dong, and B. M. Williams, "High resolution corneal and single pulse imaging with line field spectral domain optical coherence tomography," Opt. Express **24**(11), 12395 (2016).
11. L. Han, B. Tan, and Z. Hosseinaee, "Line-scanning SD-OCT for in-vivo, non-contact, volumetric, cellular resolution imaging of the human cornea and limbus," Biomed. Opt. Express **13**(7), 4007 (2022).
12. J. P. Rolland, K. S. Lee, P. Meemon, *et al.*, "Gabor domain optical coherence microscopy of human skin," in *Advances in Dermatological Sciences*, R. Chilcott and K. R. Brain, eds. (The Royal Society of Chemistry, 2013), pp. 37–52.
13. C. Canavesi and J. P. Rolland, "Ten years of Gabor-domain optical coherence microscopy," Appl. Sci. **9**(12), 2565 (2019).

Biomedical Optics EXPRESS

14. A. Dubois, W. Xue, and O. Levecq, "Mirau-based line-field confocal optical coherence tomography," Opt. Express **28**(6), 7918 (2020).
15. W. Xue, J. Ogien, and P. V. Bulkin, "Mirau-based line-field confocal optical coherence tomography for three-dimensional high-resolution skin imaging," J. Biomed. Opt. **27**(08), 1 (2022).
16. D. F. Murphy and D. A. Flavin, "Dispersion-insensitive measurement of thickness and group refractive index by low-coherence interferometry," Appl. Opt. **39**(25), 4607 (2000).
17. A. Hirai and H. Matsumoto, "Low-coherence tandem interferometer for measurement of group refractive index without knowledge of the thickness of the test sample," Opt. Lett. **28**(21), 2112 (2003).
18. P. V. Volkov, A. V. Goryunov, A. Y. Luk'yanov, *et al.*, "Measurements of the semiconductor substrate thickness with a low-coherence tandem interferometer at a nonstationary temperature," Tech. Phys. Lett. **41**(2), 110–112 (2015).
19. A. Winarno, S. Takahashi, H. Matsumoto, *et al.*, "A new measurement method to simultaneously determine group refractive index and thickness of a sample using low-coherence tandem interferometry," Precis. Eng. **55**, 254–259 (2019).
20. A. Dubois, L. Vabre, A.-C. Boccara, *et al.*, "High-resolution full-field optical coherence tomography with a Linnik microscope," Appl. Opt. **41**(4), 805 (2002).
21. A. Dubois and A. Boccara, "Full-field optical coherence tomography," in *Optical Coherence Tomography. Biological and Medical Physics, Biomedical Engineering*, W. Drexler and J. Fujimoto, eds. (Springer, 2008).
22. W. Oh, B. Bouma, and N. Iftimia, "Spectrally-modulated full-field optical coherence microscopy for ultrahigh-resolution endoscopic imaging," Opt. Express **14**(19), 8675 (2006).
23. H. D. Ford and R. P. Tatam, "Fibre imaging bundles for full-field optical coherence tomography," Meas. Sci. Technol. **18**(9), 2949–2957 (2007).
24. A. Latrive and A. C. Boccara, "In vivo and in situ cellular imaging full-field optical coherence tomography with a rigid endoscopic probe," Biomed. Opt. Express **2**(10), 2897 (2011).
25. A. Latrive, "Tomographie de cohérence optique plein champ pour l'endoscopie : microscopie in situ et in vivo des tissus biologiques," PhD Thesis (2012).
26. E. Benoit A La Guillaume, F. Martins, C. Boccara, *et al.*, "High-resolution handheld rigid endomicroscope based on full-field optical coherence tomography," J. Biomed. Opt. **21**(02), 1 (2016).
27. Y. Tang and W. Gao, "High-contrast handheld FFOCT system for tissue imaging," Opt. Lett. **49**(4), 1081 (2024).
28. S. Kim, M. Crose, and W. J. Eldridge, "Design and implementation of a low-cost, portable OCT system," Biomed. Opt. Express **9**(3), 1232 (2018).
29. M. Kim, D. Kang, and T. Wu, "Miniature objective lens with variable focus for confocal endomicroscopy," Biomed. Opt. Express **5**(12), 4350 (2014).
30. G. Maguluri, J. Grimble, and M. Mujat, "Fiber-based hand-held RCM-OCT probe for noninvasive assessment of skin lesions and therapy guidance," Transl. Biophotonics **4**(3), e202200002 (2022).
31. D. Xu, A. G. Coleto, and B. Moon, "Cascade optical coherence tomography (C-OCT)," Opt. Express **28**(14), 19937 (2020).
32. Y. Tang and W. Gao, "Effects of orientation deviation of a beam splitter and a reference mirror on the stability of a two-interferometer-based handheld FFOCT imaging probe," Appl. Opt. **60**(20), 5942 (2021).
33. Y. Tang and W. Gao, "Optimization of the performance of hand-held FFOCT scanner," Optics and Lasers in Engineering **156**, 107091 (2022).
34. J. A. Izatt, M. A. Choma, and A.-H. Dhalla, "Theory of Optical Coherence Tomography," in *Optical Coherence Tomography*, W. Drexler and J. G. Fujimoto, eds. (Springer International Publishing, 2015), pp. 65–94.
35. K. G. Larkin, "Efficient nonlinear algorithm for envelope detection in white light interferometry," J. Opt. Soc. Am. A **13**(4), 832 (1996).
36. A. Dubois, O. Levecq, and H. Azimani, "Line-field confocal time-domain optical coherence tomography with dynamic focusing," Opt. Express **26**(26), 33534 (2018).
37. J. Ogien, O. Levecq, M. Cazalas, *et al.*, "Handheld line-field confocal optical coherence tomography for dermatology," in *Proc. SPIE 11211, Photonics in Dermatology and Plastic Surgery 2020*, B. Choi and H. Zeng, eds. (SPIE, 2020), p. 26.
38. L. Waszczuk, J. Ogien, F. Pain, *et al.*, "Determination of scattering coefficient and scattering anisotropy factor of tissue-mimicking phantoms using line-field confocal optical coherence tomography (LC-OCT)," J. Eur. Opt. Society-Rapid Publ. **19**(2), 39 (2023).
39. W. Drexler, U. Morgner, and F. X. Kärtner, "In vivo ultrahigh-resolution optical coherence tomography," Opt. Lett. **24**(17), 1221 (1999).